Facile Synthesis, Characterization, Catalytic and Photocatalytic Activity of Multiferroic $BiFeO_3$ Perovskite Nanoparticles

M Sukumar (msukumsc@gmail.com)
Anand Institute of Higher Technology https://orcid.org/0000-0002-1292-7079
M. Mathankumar
St. Michael College of Engineering and Technology
Chandra Sekhar Dash
Centurion University of Technology and Management
M. Sundararajan
Paavendhar College of Arts & Science
Mohd Ubaidullah
King Saud University
Shoyebmohamad F. Shaikh
King Saud University
A. Sutha
Panimalar Engineering College
MdKausar Raza
California Institute of Technology
JoshuvaArockia Dhanraj
California Institute of Technology

Research Article

Keywords: Microwave combustion, BiFeO3 nanoparticles, Ferromagnetic behavior, Glycerol oxidation, Photocatalytic degradation of RhB

Posted Date: January 14th, 2022

DOI: https://doi.org/10.21203/rs.3.rs-1250457/v1

Abstract

We report the synthesis of multiferroic $BiFeO_3$ perovskite nanoparticles using the microwave combustion technique. Phase evolution is investigated by X-ray diffraction (XRD), which confirms that the formation of a secondary α-Bi_2O_3 phase with a monoclinic structure along with the existing rhombohedral ($BiFeO_3$) structure. The average crystalline size has been found at 50 nm. The optical band gap was calculated from the Tauc's plot it has been found 2.18 eV, as measured by diffuse reflectance spectroscopy (DRS). The appearances of Fourier transform infrared spectroscopy (FT-IR) absorption bands at 550 and 444 cm^{-1} were correlated to the rhombohedral stretching modes of bismuth ferrite nanostructure. The morphology observations using scanning electron microscopy (SEM) showed the formation of nanosized grains with pores. Energy-dispersive X-ray analysis (EDX) was done to confirm the extent of Bi^{3+}, Fe^{3+}, and O^{2-} in the samples. The magnetization-Field (M-H) hysteresis curves recorded from the vibrating sample magnetometer (VSM) revealed the appearance of ferrimagnetic behavior at room temperature. The specific surface area characterized by N_2 adsorption-desorption isotherm is found 44.86 m^2 g^{-1} using Brunauer-Emmett-Teller (BET) technique. The as-fabricated $BiFeO_3$ perovskite nanoparticles were investigated for their superior catalytic activity in two applications, which include (i) the conversion of glycerol to formic acid in a selective liquid phase batch reactor at atmospheric pressure. This bismuth-based nanoparticles exhibit as an efficient multifunctional catalyst with high conversion and selectivity efficiency around 99.2% and 98.5%, respectively, (ii) the photocatalytic degradation of rhodamine B under visible light irradiation is found maximum efficiency (99.9%), when a small amount of H_2O_2 was added during photocatalysis, indicating the samples possessed photo-Fenton like catalytic activity. Finally, we concluded that the $BiFeO_3$ perovskite nanoparticles' high performance in future multifunctional devices is demonstrated by the simultaneous enhancement of catalytic and photocatalytic activities.

1. Introduction

Multiferroic materials have received a lot of attention in recent years because of their various applications in spintronics, sensors, and novel magneto-electric devices. They have ferroic properties like ferroelasticity, ferroelectricity, and antiferro/ferromagnetism, but they are also coupled with electric, magnetic, and structural order parameters. This material necessitates the use of vacant and/or partially filled transition metal like d-orbitals, which exhibit distinctive features [1–7]. The catalytic oxidation of alcohols to carbonyl molecules is one of the most prevalent forms of oxidation reactions in organic chemistry. In the production of fine molecules and intermediates, selective catalytic oxidation is crucial. From both synthetic and industrial standpoint, liquid-phase catalytic oxidation of alcohols might be a highly appealing process for the production of intermediates and fine compounds. The catalytic conversion of primary alcohols to aldehydes is an important laboratory and industrial process [8, 9]. Furthermore, contemporary scientific study has focused on innovative visible light photo catalysts based on semiconductors in order to fulfill escalating environmental pollution and energy requirements through efficient solar energy usage. Photo-catalysis based on semiconductors has attracted a lot of interest because of its potential applications in solar energy consumption and environmental cleanup [10, 11].

The general chemical formula for perovskites is ABO_3 or A_2BO_4. In ABO_3 (A cation of larger size than B) structure, where A-site trivalent cation is 12-fold coordinated, the B-site trivalent cation is 6-fold coordinated and O is an oxygen anion. In the realm of heterogeneous catalytic reactions, they are perhaps the most researched mixed-oxide system [12, 13]. Because of their low cost, thermo-chemical stability at relatively high temperatures, and catalytic and photocatalytic activity, these perovskite oxides appear to be a potential alternative to noble metal catalysts [14]. Although these perovskite oxides are the most common and fascinating compounds, it also crystallizes in carbides, nitrides, halides, and hydrides [15]. Due to their distinctive crystal structures as well as physical and chemical characteristics, perovskite materials have attracted a lot of attention for their potential uses in solar cells, fuel cells, electro-catalysis, energy storage, catalysis, photocatalysis and so on [16]. The perovskite oxides has been studied as various catalysts such as oxidation of carbon monoxide (CO), decomposition of nitrogen oxide (NO) and NO + CO reduction and so on [17–20]. On the other hand, the perovskite oxides has been widely used for photo catalytic degradation such as organic pollutants/dyes, methyl orange, methylene blue and so on [10, 11 21]. Type 1: suprafacial, in which the catalyst surface provides a set of electronic orbitals with proper symmetry and energy for reactant and intermediate bonding; type 2: intrafacial, in which the catalyst acts as a reagent that is partially consumed and regenerated in a series of continuous redox cycles [17].

$BiFeO_3$ perovskite nanoparticles are characterized as combinations of two or more constituent minerals or phases and are well-known for their excellent thermal stability, high strength, chemical resistance, and increased catalytic characteristics [9]. Despite the abundance of nanoparticles accessible, the combination of perovskite-based metal oxide is rare in the literature. Bismuth-based perovskite nanoparticles may be produced using a variety of physical and chemical methods, including sol-gel [8], solid-state reaction [22], sonochemical approach [1], and hydrothermal method [23]. Sensors, catalytic activities, photocatalytic activities, and spintronics devices utilizes $BiFeO_3$ perovskite-type oxides [11, 22].

Ramezanalizadeh et al. used a modified sol-gel approach to make $BiFeO_3$ perovskite oxide. The gel was formed using 2-methoxyethanol and acetic acid, and then baked at 80 ^oC for 12 hours before being annealed at 600 ^oC for 30 minutes in air or N_2. The oxidation of primary and secondary alcohols was achieved using this perovskite oxide [8]. On the other hand, *Li* et al. have prepared $BiFeO_3$ perovskite by employing microwave-assisted hydrothermal using polyethylene glycol (PEG 6000, 4000, and 2000) as a precipitate agent then subjected to microwave irradiation at 190 ºC for 30 min followed by vacuum drying oven at 60 ºC for 12 h. These perovskite oxides have been used for the degradation of RhB [24]. However, there are few reports on the manufacture of $BiFeO_3$ utilizing a microwave aided combustion approach. The current work focuses on the microwave aided combustion technique for the synthesis of $BiFeO_3$ perovskite oxides, as well as the influence of microwave irradiation on the formation of a secondary perovskite phase (-Bi_2O_3). Microwave-assisted combustion provides several advantages over traditional heating techniques, including a faster synthesis time, lower energy usage, and the ability to fabricate materials with particular catalytic and photocatalytic characteristics. As a result, microwave-assisted methods for the production of inorganic materials are widely employed [24]. We produced $BiFeO_3$

perovskite nanoparticles and evaluated them using different methods such as XRD, DRS, FTIR, HRSEM, EDX, VSM, and BET to determine structural, optical, morphological, magnetic, and textural characteristics. The as-fabricated $BiFeO_3$ perovskite nanoparticles are reported for the first time by our group, and its multi-functional abilities towards the oxidation of glycerol and photocatalytic degradation of RhB are described in the subsequent sections.

2. Experimental

2.1. Chemicals

Iron nitrate nonahydrate ($Fe(NO_3)_3.9H_2O$), bismuth nitrate pentahydrate ($Bi(NO_3)_3.5H_2O$), L-alanine ($C_3H_7NO_2$), glycerol ($C_3H_8O_3$), and rhodamine B (RhB) are of analytical quality (99.9%) and obtained from SD fine-chemicals (India). All solutions were made using distilled water.

2.2. Synthesis of $BiFeO_3$ perovskite nanoparticles

Iron nitrate and bismuth nitrate were used as precursors and L-alanine as a fuel for the preparation of $BiFeO_3$ perovskite nanoparticles. To obtain a homogenous solution, the precursors and L-alanine components were dissolved in distilled water in the required quantities and stirred for 30 minutes at room temperature. The fuel to oxidizer ratio (F/O) was one [23] according to the propellant chemistry principle. The required amount of oxidizer-to-fuel molar ratio for the mixture was calculated using the equation (1) [9]. The homogenous solution was placed in a microwave oven (800 W, power) operating at 2.45 GHz for 10 minutes. When the precursor solution reached the threshold temperature, it was dehydrated and burnt, yielding a black fluffy powder that was calcined at 500°C for 2 hours. As a result of this, two phases are generated in the production of crystalline Bi_2O_3 and $BiFeO_3$. The prepared $BiFeO_3$ perovskite nanoparticles are evaluated for the catalytic oxidation of glycerol and photocatalytic degradation of RhB, respectively. The steps involved in the process of fabrication of $BiFeO_3$ perovskite nanoparticles is depicted schematically in Fig. 1.

$$Oxidizer/Fuel = \frac{\sum all\ oxidizing\ and\ reducing\ elements\ in\ oxidizer}{(-1)\sum oxidizing\ and\ reducing\ elements\ in\ fuel} \quad (1)$$

2.3. Characterization

The crystalline phase of the materials was investigated using Rigaku, RXIII on a D/MAX-2500 machine with CuKα radiation (λ = 1.5406 Å) in the range between from 10 ^{o} to 80^o. The UV-Vis diffuse reflectance spectra (UV-DRS) of the samples were used to estimate the optical band gap using a Thermo Scientific Evolution 300 UV-visible spectrophotometer. On a Thermo scientific Nicolet iS 10 OMNI FTIR spectrophotometer with a KBr pellet is used for sample preparation and performing Fourier transform infrared (FT-IR) studies. A high resolution field scanning electron microscope (HR-SEM, HITACHIS4800) equipped with an energy dispersive X-ray spectrometer (EDX, HORIBA EMAX) was used to examine the morphology and elemental composition of the samples. The magnetic characteristics were measured at

room temperature using a vibrating sample magnetometer (VSM, PMC MicroMag 3900 model) with a maximum field of 15 kOe. After degassing at 250 ^{o}C for 6 hours, the surface area of the catalyst was calculated using the Brunauer–Emmett–Teller (BET) technique using N_2 adsorption and desorption isotherms obtained on a Micromeritics – ASAP 2020 unit with liquid nitrogen adsorption at 77K using a PHS-1020 instrument.

2.4. Catalytic activity

Glycerol oxidation was carried out in a batch reactor under air conditions. A 250 mL two-necked round bottom flask was filled with 50 mmol of glycerol as reactant and 50 mmol of hydrogen peroxide as the oxidant. Following that, 50 mg of $BiFeO_3$ was added as a catalyst and 50 mmol of acetonitrile was added as a solvent. The mixture was stirred at 70 ºC for 6 hours. After completion of the reaction, the mixture was gradually cooled to room temperature and the catalyst was separated by filtration method. The converted products were analyzed by gas chromatography (GC) with flame ionization detector (FID), using an Agilent 7890B GC system. The main by-products were detected using an Agilent Technologies Model 7890A with mass detector model 5975C and HP-5MS column in a gas chromatography mass spectrometer (GC-MS).

2.5. Photocatalytic activity

The photocatalytic activity of $BiFeO_3$ perovskite nanoparticles were assessed for the inorganic dye (rhodamine B, RhB) degradation through visible light source (Source power: 150 W Halide lamp and wavelength is $\lambda > 420$ nm). A fixed concentration of about 0.31 g of bismuth nanoparticles was distributed in 1L of RhB dye solutions and irradiated with visible light. To induce a Fenton-like reaction, the pH of the solution was adjusted to 2 by adding the needed amount of hydrochloric acid. Previously, the solution was placed in dark condition for overnight at room temperature to attain adsorption amid RhB dye solution and $BiFeO_3$ perovskite nanoparticles. In photoreaction, air was expelled for dispersing $BiFeO_3$ perovskite catalyst in the solution. $1x10^{-6}$ L of 30% H_2O_2 was added to the 1L of dye solution to produce additional hydroxide radicals ($OH^{\bullet}$) through the photo-degradation, for speedy oxidation. UV-Vis spectra were recorded for time intervals, before and after photocatalytic degradation.

3. Results And Discussion

3.1. XRD analysis

Figure 2 displays the XRD patterns of $BiFeO_3$ at room temperature. The XRD peaks belong to rhombohedral structure $BiFeO_3$ (space group $R3c$ and JCPDS card No: 86-1518) and the main byproducts were α-Bi_2O_3, it belong to monoclinic structure (space group $P2_1/c$, JCPDS No: 76-1730) as indicated with the red arrows. The prominent Bragg reflections planes were observed at 2θ values around 22.4º, 31.7º, 32.0º, 37.6º, 38.9º, 39.4º, 45.7º, 51.3º, 51.7º, 56.3º, 57.1º, 66.3º, 67.0º, 70.6º, 71.6º, 75.6º and 76.1º, which are assigned to the (012), (104), (110), (113), (006), (202), (024), (116), (112), (018), (300), (208),

(220), (131, 1010), (312), (128) and (134) crystallographic planes respectively, which corroborates with the aforementioned JCPDS card number well. The average crystallite size of $BiFeO_3$ perovskite nanostructures was found to be 50 nm, determined by means of Debye-Scherrer formula [26]. According to the XRD results, the lattice parameters and cell volume of the rhombohedral $BiFeO_3$ perovskite nanostructure were *a* = 5.5770, *c* = 13.861 and *V* = 384.12.

3.2. Optical properties

UV–Vis diffuse reflectance spectroscopy was used to investigate the optical characteristics of $BiFeO_3$ perovskite (Fig. 3a). The Kubelka–Munk (K–M) function is commonly used to transform diffuse reflectance into comparable absorption coefficients, as shown in equation (2), and is commonly employed for powder sample analysis.

$$\alpha = F(R) = \frac{(1-R)^2}{2R} \qquad (2)$$

where, *F(R)* is the K–M function and *R* is the reflectance. Thus, to calculate optical energy band gap as modified Tauc relation equation is $ahv = A(hv - Eg)^n$, where *a* is the absorption coefficient, *h* is Planck's constant, *A* is the constant, E_g is the optical energy band gap and for direct transitions n = 1/2. A graph is plotted between $(F(R)hv)^2$ *vs hv*, which upon extrapolation of the linear region *to* $(F(R)hv)^2 = 0$ gives the optical energy band gap value. The optical energy band gap of the $BiFeO_3$ perovskite nanostructure is 2.18 eV, which is lower than previously reported values of 2.27 eV and 2.25 eV in [25, 26], perhaps due to quantum confinement processes at the nano-regime [29].

The optical band edge potential namely conduction band (CB) and valence band (VB) edge potential of $BiFeO_3$ nanoparticles were determined using equation (3) and (4).

$$E_{CB} = X - E^C - 0.5E_g \quad (3)$$

$$E_{VB} = E_{CB} + E_g \quad (4)$$

The calculated CB edge potential versus NHE for bismuth ferrite is 0.302 eV. Similarly VB edge of bismuth ferrite is 2.25 eV.

3.3. FT-IR analysis

The chemical bonding information of the $BiFeO_3$ perovskite nanostructures was evaluated using Fourier transform infrared spectroscopy (FTIR) at 303 K. The formation of rhombohedral perovskite structure and the presence of surface functional groups were confirmed using FTIR spectrum investigation, which is plotted in the region of 4000 to 400 cm^{-1} as shown in Fig. 3b. The O-H longitudinal stretching vibration of the adsorbed water molecules is related with the wide band centered at 3427 cm^{-1}. The C-H asymmetric and symmetric stretching vibrations were related with the band around 2922 cm^{-1}, whereas the H–O–H bond vibration was linked to the band around 1631 cm^{-1}.Due to the combustion procedures, the weak

bonds at 1383 and 1115 cm^{-1} might be ascribed to leftover nitrogen groups. Furthermore, the metal oxide (bismuth and iron) stretching modes of rhombohedral $BiFeO_3$ perovskite nanostructure are related to the distinctive absorption bands at 550 and 444 cm^{-1} [30].

3.4. HR-SEM and EDX analysis

The electronic micrographs produced using the high resolution scanning electron microscopy (HR-SEM) technique is shown in Fig. 4a. The produced $BiFeO_3$ perovskite nanoparticles exhibit a dense morphology of sphere-like form with intragranular holes, pore walls that are merged grains with defined grain boundaries. The average particle size calculated from the HR-SEM picture of the $BiFeO_3$ perovskite nanostructure is about 43 nm, which differs somewhat from the crystallite size determined by XRD measurements. Because the diffracting domain size in the nanoparticle is linked to aggregated cluster size, the former is used. The energy dispersive X-ray analysis was used to analyze the elements in this sample (EDX). The chemical composition of the $BiFeO_3$ perovskite nanostructure roughly matches the nominal composition 1: 1: 3, and the existence of Bi, Fe, and O components has been established. As illustrated in Fig. 4b, the observed quantitative values reveal atomic percentages of bismuth, iron, and oxygen (inset table).

3.5. Magnetic studies

At room temperature, the magnetic characteristics of $BiFeO_3$ perovskite nanoparticles were measured. Figure 5a shows the magnetic hysteresis (M-H) loop curves for $BiFeO_3$ perovskite samples. The $BiFeO_3$ perovskite nanoparticles exhibit a ferromagnetic behavior with the saturation magnetization (M_s), remanence (M_r) and coercivity (H_c) values are 38.27 memu/g, 10.89 memu/g and 198.03 Oe respectively. The suppression of the known spiral (cycloidal) spin structure with a period of around 62 nm and uncompensated spins at the nanoscale can be attributed to the saturation magnetization value reported in $BiFeO_3$ perovskite nanoparticles [31, 32]. $BiFeO_3$ has G-type anti-ferromagnetic ordering with a linear applied field dependency of magnetization. However these types of perovskite nanoparticles have weak ferromagnetism due to the disruption of the long-range anti-ferromagnetic order at the particle surface [33, 34]. Furthermore, in nanoparticles with a high surface-to-volume ratio, there are more uncompensated spins from the particle surface, causing magnetization to develop. The size impact of the nanoparticles may also be responsible for the improved magnetic characteristics. A similar observation was previously reported [31]. The magnetic recovery of the catalysis and photocatalyst after degradation can be aided by the ferromagnetism behavior of $BiFeO_3$ perovskite nanoparticles.

3.6. N_2 adsorption–desorption isotherms

Figure 5b illustrates the nitrogen adsorption-desorption isotherms of $BiFeO_3$ perovskite nanoparticles and also presents the specific surface area (S_{BET}), pore diameter (D_P), pore volume (V_P) and equivalent particle size (D_{BET}), recorded at 77 Kelvin using the Brunauer–Emmett–Teller (BET) technique. According to the International Union of Pure and Applied Chemistry (IUPAC), the particle agglomerations have a typical type II isotherm. The obtained type II isotherm was recorded at high relative pressure designating

the formation of mesopores in the $BiFeO_3$ perovskite nanoparticles [35]. The textural property of $BiFeO_3$ perovskite such as the surface area and pore diameter were reported to be 44.860 $m^2\ g^{-1}$ and 4.319 nm respectively. The greater pore volume (VP – 0.104 cc g^{-1}) was caused by the higher surface area of $BiFeO_3$, which is ascribed to the formation of additional gaseous products during the synthesis process. The textural features of the $BiFeO_3$ perovskite has acceptable porosity and surface area for catalytic and photocatalytic applications [9].

3.7. Catalytic activities

3.7.1. Catalytic activities of $BiFeO_3$ perovskite nanoparticles

The multiferroic material of $BiFeO_3$ perovskite nanostructures have been evaluated for the catalytic oxidation of glycerol in liquid phase batch reactor under air conditions. According to the GC-MS data in Fig. 6, the catalytic conversion of glycerol and the selectivity of formic acid were determined to be 99.2 percent and 98.5 percent, respectively. BET methods revealed that the $BiFeO_3$ catalyst had the highest catalytic activity due to its large surface area.

3.7.2. Effect of catalyst loading

Figure 7a illustrates the amount of catalyst loading (10 to 70 mg) on the oxidation of glycerol using $BiFeO_3$ perovskite nanoparticles at 70 ºC for 360 minutes. Gradually increasing the catalyst dosage from 10 to 50 mg, increased the proportion of glycerol conversion (61 to 99 percent) and selectivity (55 to 98 percent). Moreover 50 mg of catalyst loading causes a dramatic fall in conversion (87%) and selectivity (84%), which is comparable to the values reported in literature [36, 37]. It is due to pore clogging of the catalyst surface, which leads to decrease in reactive surface area accessible to progress the reaction [29]. For the oxidation of glycerol to formic acid, a catalyst dosage of 50 mg achieves good catalytic activity.

3.7.3. Recycling test

The reusability ability was importantly essential for the economic feasibility of reaction. The possibility of recycling performance was also investigated under the optimal reaction parameters. Following the first trail, the catalyst was collected, filtered, and washed multiple times with de-ionized water before being dried in a hot air oven at 120 ^oC for 120 minutes. After recycling for four runs under identical reaction a condition. According to the data (Fig. 7b), there is a minor decrease in the percentage of glycerol conversion and selectivity of formic acid, which is related to a slight mass loss during the catalyst recovery process [38, 39].

3.7.4. Reaction pathway

The proposed reaction pathway of glycerol to formic acid over a $BiFeO_3$ perovskite catalyst in an acetonitrile medium is shown in Fig. 8. Arcanjo et al. [40], Lihua Yang et al. [41], Chun Ho Lam et al. [42], Sukumar et al. [9, 36] and Haider et al. [43] earlier reported that it is a two-path sequential reaction. The first pathway involves the oxidative dehydrogenation to form either glyceraldehyde or hydroxyacetone.

The glyceraldehyde was further oxidized to glyceric acid. Furthermore, oxidized at the three-carbon leads to form tartronic acid. If would broke its C-C bond splitting quickly, to form glycolic acid and formic acid. Then, hydroxyacetone was oxidized to form 2-hydroxypropenal towards the pyruvaldehyde, which goes through rearrangement to form lactic acid. The second pathway, which is followed by hydroxyacetone and involves radical fragmentation, is similar to the Norrish type I process, and involves C-C bond cleavage to produce acetaldehyde and methanol precursors. Acetaldehyde is metabolized to acetic acid subsequently. Methanol, on the other hand, is oxidized to generate formaldehyde, which is further oxidized to form formic acid due to the loss of hydrogen radical.

3.8. Photocatalytic degradation of RhB dye solution over $BiFeO_3$ perovskite nanoparticles

3.8.1. Effect of time

Figure 9a depicts UV-visible light spectra for the extent of photocatalytic degradation of RhB at optimized conditions 6 mg/l, pH is 2 over the irradiation. The characteristics absorption wavelength peaks at 503 nm for de-ethylated and 558 nm tetra ethylated RhB molecule [44, 45]. Control experiments were done in the dark; it was observed that after complete adsorption process there is no decrease in intensity peak. It suggests that upon addition of hydrogen peroxide (H_2O_2) there is no degradation took place after 165 minutes. Fig. 9b, indicates the photocatalytic activity of $BiFeO_3$ perovskite catalyst kept in dark condition, where complete degradation of RhB using $BiFeO_3$ perovskite catalyst with 6 mg/l of dye solution at 165 minutes under visible light radiation. The photocatalytic activity of $BiFeO_3$ perovskite nanoparticles achieves excellent photo-degradation. It is attributed to the recombination and separated electron/hole (e^-/h^+) pairs and also easily available for the oxidation process, which means in terms of the charge carriers. The illumination of visible source with respect to time, leads to gently change in the color of RhB dye solution. The color changed from pink to colorless, which corresponds to the destruction of chromophoric group.

3.8.2. Efficiency and recycle performance

As shown in Fig. 9c, the effect of $BiFeO_3$ perovskite nanoparticles photocatalytic degradation efficiency was evaluated at an RhB concentration of 6 mg/l and a pH of 2. After 165 minutes, the photocatalytic degradation efficiency of $BiFeO_3$ was found to be 99.9%, owing to the efficient separation and suppression of electron-hole pair recombination, as well as the geometric and electronic structures of bismuth ferrite. The stability of the $BiFeO_3$ perovskite catalyst, as shown in Fig. 9d, even after five cycles with no decline of photocatalytic degradation efficiency.

3.8.3. Mechanism of dye degradation

Figure 10 showed the possible photocatalytic degradation mechanism for the $BiFeO_3$ perovskite catalyst under visible light illumination. The e^-/h^+ pairs are created in $BiFeO_3$ perovskite nanoparticles. These photo-generated h^+/e^-pairs facilitate the oxidation and reduction process of RhB in aqueous solution. In

$BiFeO_3$, the conduction band (CB) edge is at ca 0.302eV the valence band (VB) edge is at ca 2.482 eV and against normal hydrogen electrode (NHE). In this process, the CB edge value is less than redox potential of $O_2/O_2^{\bullet -}$ (-0.33 V). This avert the electron in the CB and react to O_2 with produce the ($O_2^{\bullet -}$) which is also a strong oxidant. Hence, not fit for reduction process. Further, the electron in CB of catalyst surface react with H_2O_2 to produce $OH^{\bullet}$ radical which is responsible for the degradation of RhB dye. Beside, hole direct oxidation of the RhB molecules and has higher oxidation potential.

The redox potential of $OH^{\bullet}/OH^-$ (1.99 V), which was compared to valance band edge of $BiFeO_3$ is more positive. This photo-generated positive holes can oxidize water (H_2O) that will take formation of OH^- to form $OH^{\bullet}$ radical due to large peak shift in the peak and de-ethylation of RhB molecule. The oxidant of ozone and hydrogen peroxide for RhB solution is the $OH^{\bullet}$ radicals have higher oxidation potential. In this process holes, led to decolouration and de-ethylation, thereby degradation of RhB. The $BiFeO_3$ perovskite, the Fe^{3+} cation which is present on the surface of catalyst likewise react with hydrogen peroxide, thus producing a Fenton-like process which is a most powerful tool and resulting in peroxide $^{\bullet}OOH$ and $OH^{\bullet}$ radical. Also, H_2O_2 react with Fe^{3+} ion surface of the catalyst could seize the electrons form $OH^{\bullet}$ radicals from the $BiFeO_3$ system [46, 47]. The weakness of recombination of e^-/h^+ pairs, leads to improve photocatalytic degradation efficiency.

RhB + hυ (visible light) → RhB dye* (5)

RhB dye * + $BiFeO_3$ → RhB dye^{*+} + $BiFeO_3$ (e^-) (6)

H_2O_2 + $BiFeO_3$ (e^-) → OH^- + $OH^{\bullet}$ (7)

RhB dye^{*+} + $OH^{\bullet}$→ degradation products (8)

4. Conclusion

In summary, an integral analysis and discussion of the synthesis pathway and structural, optical, morphological, magnetic, textural, catalytic, and photocatalytic activities are provided in this paper. The use of L-alanine as fuel in the $BiFeO_3$ perovskite synthesis produces nanoparticles. The crystal structure was identified to be rhombohedral structure with $R3c$space group with crystallite size around 50 nm. In addition, the main byproduct formed is the α-Bi_2O_3 phase. The optical band gap value of $BiFeO_3$ perovskite nanoparticles was 2.18 eV. The vibrational stretching modes of the $BiFeO_3$ perovskite rhombohedral structure are validated by FT-IR investigation. Morphological analyses show that the intragranular porosity is highly developed, with discrete grains on the surfaces. At room temperature, magnetic measurements show the advent of ferromagnetic activity. With aid of Brunauer-Emmett-Teller (BET) method mesopores were observed with type II isotherms, which have large surface area of 44.86 m^2/g of the $BiFeO_3$ perovskite nanostructure. Subsequently, the $BiFeO_3$ perovskite nanoparticles were

investigated for superior catalytic activity in two applications; as follows (i) Glycerol to formic acid oxidation in the liquid phase with a high efficiency of over 98 percent, (ii) Under visible light, the photocatalytic breakdown of rhodamine B achieved maximal efficiency (almost 99 percent). The mechanics of two applications are described in detail and our results demonstrated high catalytic activity in diverse applications.

Declarations

Acknowledgement

The authors are grateful to be the Researchers supporting Project number (RSP-2021/370), King Saud University, Riyadh, Saudi Arabia for the support.

References

1. P. Dimple, B.P. Dutta, R. Mandal, G. Naik, Lawes, A.K. Tyagi, J. Phys. Chem. C **117**, 2382–2389 (2013)
2. D. Paritosh Modak, Lahiri, S.M. Sharma, J. Phys. Chem. C **120**, 15, 8411–8416 (2016)
3. X. Weiwei Mao, L. Wang, Y. Chu, Q. Zhu, J. Wang, Zhang, Jianping Yang, Xing'ao Li and Wei Huang. Phys. Chem. Chem. Phys. **18**, 6399–6405 (2016)
4. L. Renqing Guo, W. Fang, F. Dong Zheng and M. Shen, J. Mater. Chem. **21**, 18645–18652 (2011)
5. M. Agila, S. Krithiga, Int. j. eng. sci. manag. res **2**, 475–482 (2019)
6. S. Haq, W. Rehman, M. Rehman, J. Inorg. Organomet. Polym Mater. **30**, 1197 (2020)
7. S. Shoukat, S. Haq, W. Rehman, M. Waseem, M. Hafeez, S.U. Din, P. Zain-ul-Abdin, M. Ahmad, A. Ur Rehman, B. Shah, Khan, J. Inorg. Organomet. Polym. Mater. 1 (2020)
8. H. Ramezanalizadeh, F. Manteghi, RSC Adv. **6**, 99096–99104 (2016)
9. M. Sukumar, L. John Kennedy, J. Judith Vijaya, B. Al-Najar, M. Bououdina, New J. Chem. **42**, 18128–18142 (2018)
10. D. Sen Wang, F. Chen, N. Niu, L. Zhang, Y. Qin, Huang, J. Alloys Compd. **688**, 399–406 (2016)
11. B. Safizade, S.M. Masoudpanah, M. Hasheminiasari, A. Ghasemi, RSC Adv. **8**, 6988–6995 (2018)
12. D. Sébastien Royer, F. Duprez, X. Can, Courtois, Catherine Batiot-Dupeyrat, Said Laassiri, and Houshang Alamdari. Chem. Rev. **114**, 10292–10368 (2014)
13. J. Zhu, H. Li, L. Zhong, P. Xiao, X. Xu, X. Yang, Z. Zhao, J. Li, ACS Catal **4**, 2917–2940 (2014)
14. A. Civera, M. Pavese, G. Saracco, V. Specchia, Catal. Today **83**, 199–211 (2003)
15. M.A. Pena, J.L.G. Fierro, Chem. Rev. **101**, 1981–2017 (2001)
16. C.-J. Ma, N. Li, L.-L. Chen, H. Chen, W.-L. Song, J. Phys. Chem. Lett. **12**, 4104–4111 (2021)
17. J. Zhu, Z. Zhao, D. Xiao, J. Li, X. Yang, Y. Wu, Ind. Eng. Chem. Res. **44**, 4227–4233 (2005)
18. H. Falco´n, M.J. Martinez-Lope, J.A. Alonso, J.L.G. Fierro, Appl. Catal. B **26**, 131–142 (2000)

19. Y. Teraoka, T. Harada, S. Kagawa, J. Chem. Soc., Faraday Trans **94**, 1887–1891 (1998)
20. V.C. Belessi, T.V. Bakas, C.N. Costa, A.M. Efstathiou, P.J. Pomonis, Appl. Catal. B **28**, 13–18 (2000)
21. O.P. Bajpai, S. Mandal, R. Ananthakrishnan, P. Mandal, D. Khastgir, S. Chattopadhyay, New J. Chem. **42**, 10712–10723 (2018)
22. M. Sverre, M.-A. Selbach, T. Einarsrud, Tybell, T. Grande, J. Am. Ceram. Soc. **90**, 3430–3434 (2007)
23. Z. Tong Gao, F. Chen, D. Niu, Q. Zhou, Y. Huang, L. Zhu, X. Qin, S.Y. Huang, J. Alloys Compd. **648**, 564–570 (2015)
24. S. Li, G. Zhang, H. Zheng, N. Wang, Y. Zheng, P. Wang, RSC Adv. **6**, 82439–82446 (2016)
25. M. Sukumar, L. John Kennedy, J. Nanosci. Nanotechnol. **19**, 826–832 (2019)
26. M. Sukumar, L. John Kennedy, J. Judith Vijaya, B. Al-Najar, M. Bououdina, Gopinath Mudhana **167**, 407–415 (2019)
27. José Luis Ortiz-Quiñonez, D. Díaz, Inti Zumeta-Dubé, Humberto Arriola-Santamaría, Israel Betancourt, Patricia Santiago-Jacinto, and Noel Nava-Etzana, Inorg. Chem. 2013, 52, 10306–10317
28. S. Ayan Mukherjee, N. Chakrabarty, W.-N. Kumari, Su, S. Basu, ACS Omega **3**, 5946–5957 (2018)
29. M. Sukumar, L. John Kennedy, J. Judith Vijaya, B. Al-Najar, M. Bououdina, Ceram. Int. **44**, 18113–18122 (2018)
30. S. Chaturvedi, R. Das, P. Poddar, S. Kulkarni, RSC Adv. **5**, 23563–23568 (2015)
31. K.P. Remya, R. Rajalakshmi, N. Ponpandian, Nanoscale Adv. **2**, 2968–2976 (2020)
32. P. Dimple, B.P. Dutta, R. Mandal, G. Naik, Lawes, A.K. Tyagi, J. Phys. Chem. C **117**, 2382–2389 (2013)
33. T.-J. Park, G.C. Papaefthymiou, J. Arthur, A.R. Viescas, Moodenbaugh, S.S. Wong, Nano Lett. **7**, 766–772 (2007)
34. B. Safizade, S.M. Masoudpanah, M. Hasheminiasari, A. Ghasemi, RSC Adv. **8**, 6988–6995 (2018)
35. A. Katie, Cychosz, Remy Guillet-Nicolas, Javier Garcia-Marinez and Matthias Thommes. Chem. Soc. Rev. **46**, 389–414 (2017)
36. M. Sukumar, L. John Kennedy, J. Judith Vijaya, B. Al-Najar, M. Bououdina, Mater. Sci. Semicond. Process. **100**, 225–235 (2019)
37. S. Thanasilp, J.W. Schwank, V. Meeyoo, S. Pengpanich, M. Hunsom, Chem. Eng. J. **275**, 113–124 (2015)
38. Z.I. Ishak, N.A. Sairi, Y. Alias, M.K.T. Aroua, R. Yusoff, Chem. Eng. J. **297**, 128–138 (2016)
39. K.-X. Li, L. Chen, Zong-ChengY.Hong-Lin Wang, Catal Lett. **139**, 151–156 (2010)
40. M. Rosiene, A. Arcanjo, I.J. Silva Jr.,, R.S. Vieira, Enrique Rodríguez-Castellón, Antonia Infantes-Molina. Catal. Today **279**, 317–326 (2017)
41. X. Lihua Yang, P. Li, Z. Chen, Hou, Chin. J. Catal. **40**, 1020–1034 (2019)
42. C.H. Lam, A.J. Bloomfield, P.T. Anastas, Green Chem., 2017,19, 1958–1968
43. M.H. Haider, N.F. Dummer, D.W. Knight, R.L. Jenkins, M. Howard, J. Moulijn, S.H. Taylor, G.J. Hutchings, Nat. Chem. **7**, 1028–1032 (2015)

44. M. Sundararajan, L.J. Kennedy, J. Environ. Chem. Enginner **5**, 4075–4092 (2017)
45. C. Singh, A. Goyal and S. Singhal, Nanoscale**,** 2014, 6, 7959-7970.
46. M. Sundararajan, V. Sailaja, L.J. Kennedy, J.J. Vijaya, Ceram. Inter **43**, 540–548 (2017)
47. X. Zhou, H. Yang, C. Wang, X. Mao, Y. Wang, Y. Yang, G. Liu. J. Phys. Chem. C **114**, 17051–17061 (2010)

Figures

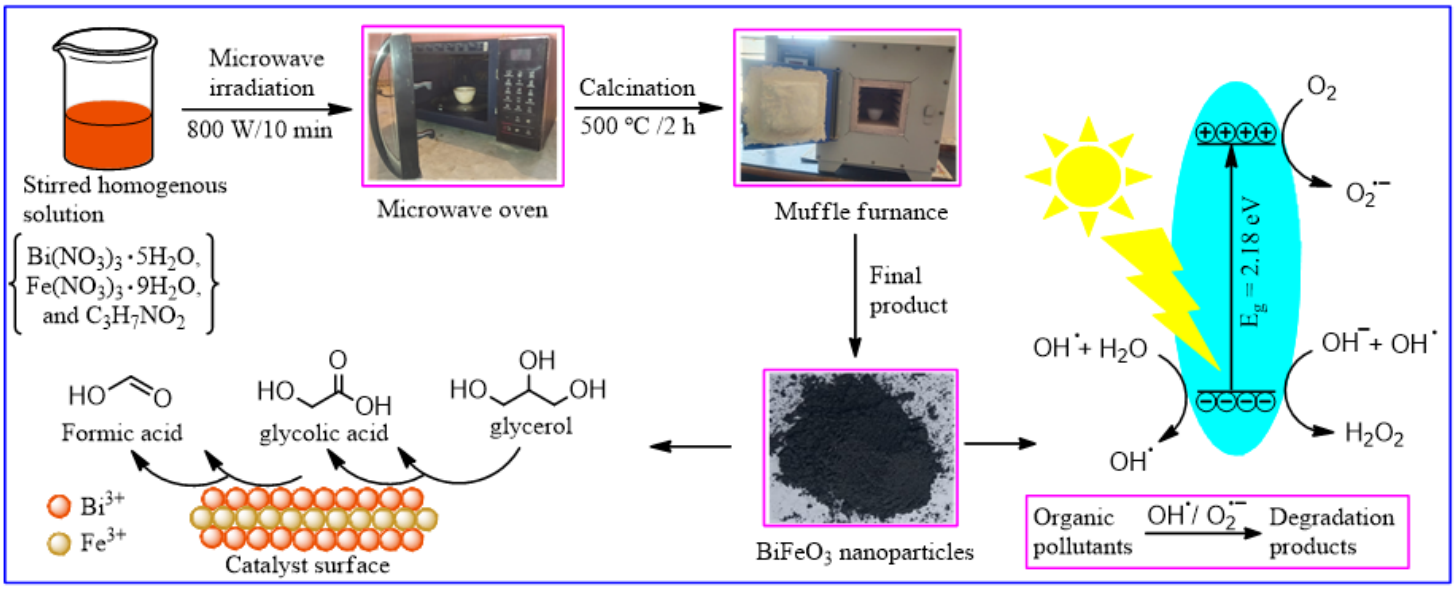

Figure 1

Schematic representation of the preparation of $BiFeO_3$ perovskite nanoparticles.

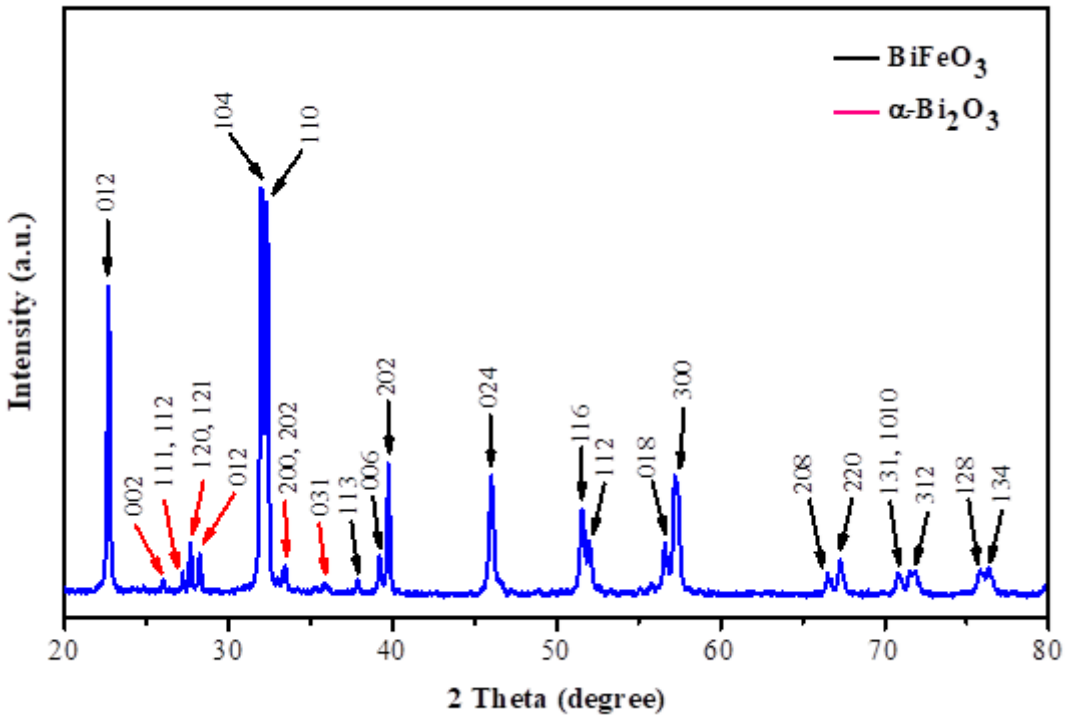

Figure 2

X-ray diffraction patterns of the $BiFeO_3$ perovskite nanoparticles.

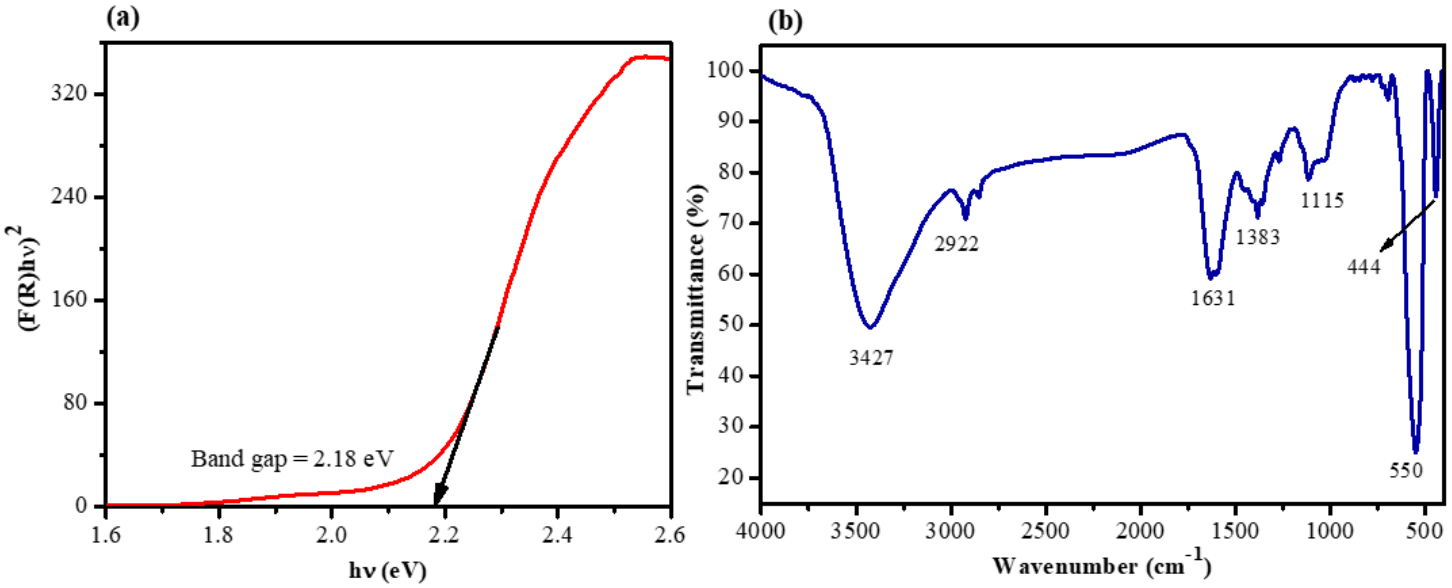

Figure 3

(a) Plot of $(F(R)hv)^2$ versus hv for the $BiFeO_3$ perovskite nanoparticles, **(b)** FT-IR spectra of the $BiFeO_3$ perovskite nanoparticles.

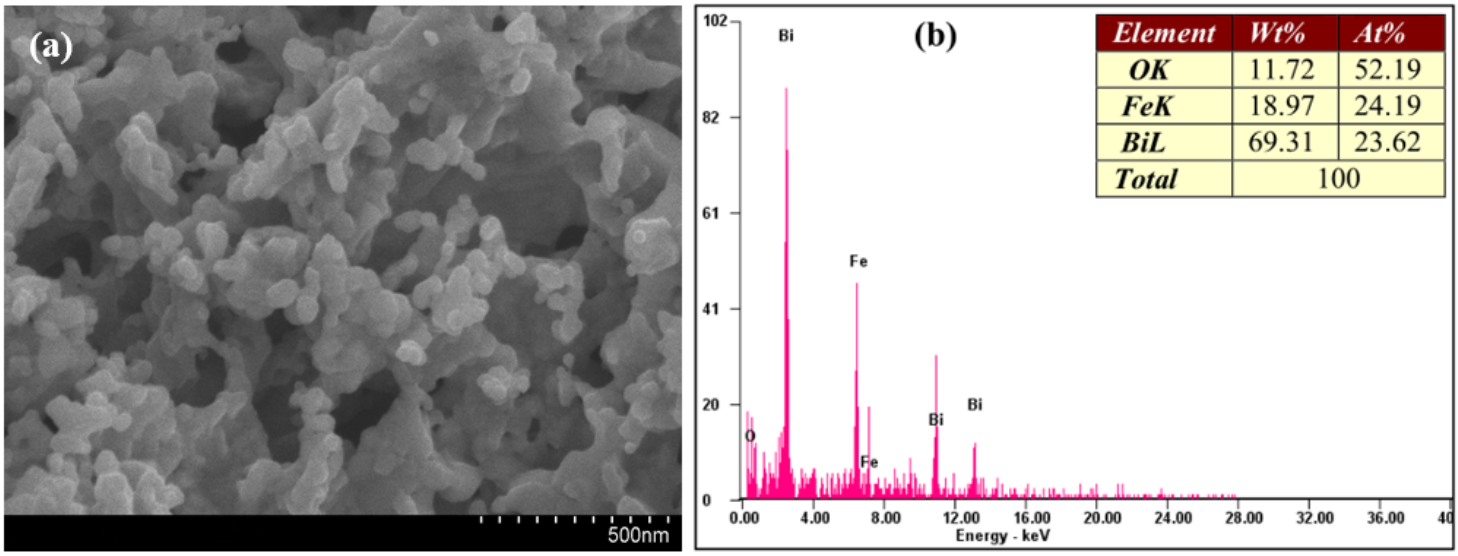

Figure 4

(a) HR-SEM image of the $BiFeO_3$ perovskite nanoparticles, **(b)** EDX spectra of the $BiFeO_3$ perovskite nanoparticles.

Figure 5

(a) Magnetic hysteresis curves of the $BiFeO_3$ perovskite nanoparticles, **(b)** N_2 adsorption–desorption isotherms obtained from the BET measurements of the $BiFeO_3$ perovskite nanoparticles.

Figure 6

GC-MS spectra of glycerol oxidation using the $BiFeO_3$ perovskite sample.

Figure 7

(a) Effect of catalyst loading on the conversion of glycerol over the $BiFeO_3$ sample.

(b) Recycling performance of the $BiFeO_3$ sample.

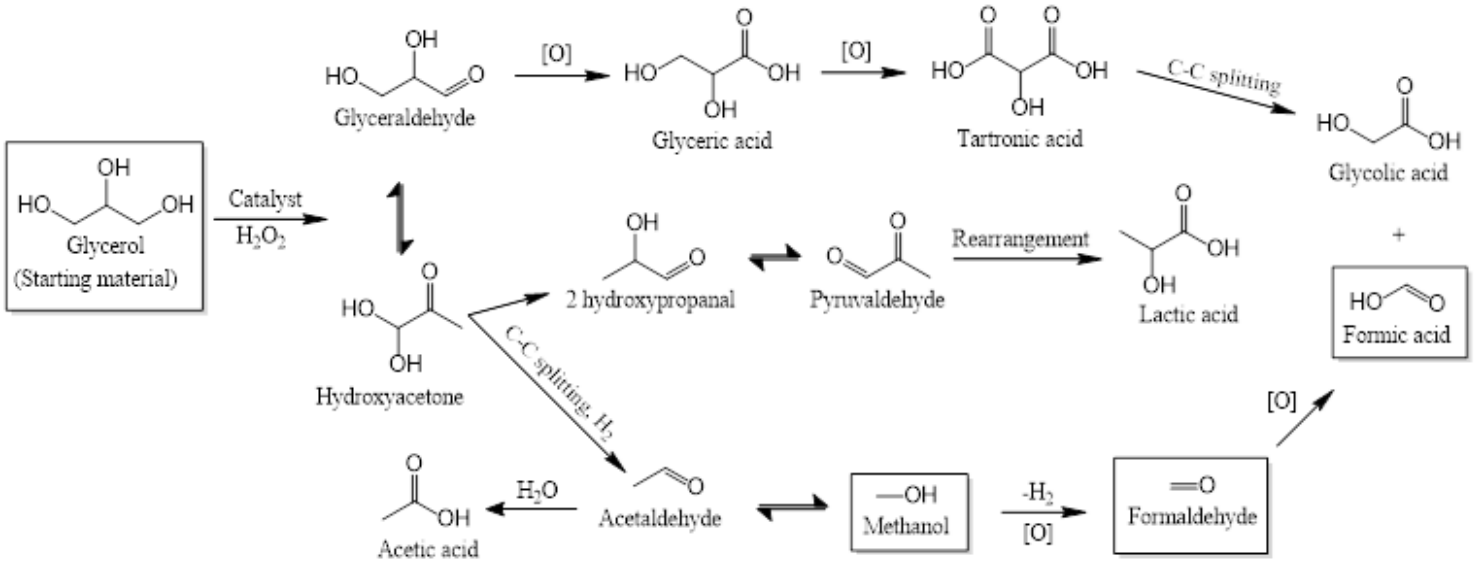

Figure 8

Possible reaction pathway for the conversion of glycerol using $BiFeO_3$ catalyst. Detected products are framed.

Figure 9

(a) Effect of time, **(b)** The plots of C_t/C_0 versus reaction time, **(c)** PCD efficiency, and **(d)** Reusability of $BiFeO_3$ catalyst for RhB on the photocatalytic degradation.

Figure 10

Mechanism of photocatalytic degradation of RhB by $BiFeO_3$ catalyst.